Proton-^{90}Zr mean field between -60 and $+185$ MeV from a dispersive optical model analysis

Y. Wang,[1,2] C. C. Foster,[2] R. D. Polak,[1,2] J. Rapaport,[3] and E. J. Stephenson[2]
[1]*Physics Department, Kent State University, Kent, Ohio 44242*
[2]*Indiana University Cyclotron Facility, Bloomington, Indiana 47408*
[3]*Physics Department, Ohio University, Athens, Ohio, 45701*
(Received 11 February 1993)

Elastic scattering of protons from ^{90}Zr in the energy range $E_p = 9.8$ to 135 MeV is analyzed using a dispersive optical model potential (OMP). In this analysis, a dispersion relation connects the volume integrals of the imaginary and the real parts of the OMP. Best-fit dispersive OMP parameters are obtained from fits to experimental cross section and analyzing power data at each energy, while the volume integrals of the imaginary potential and dispersive correction terms are fixed at the empirical values obtained in the individual proton elastic scattering analyses from 9.8 to 135 MeV. Predictions of the cross section and analyzing power angular distributions from the best-fit dispersive OMP and conventional OMP are obtained, and give similar quality fits to data. A dispersive OMP with parameters that show a smooth energy dependence are determined from fits to the entire data set. Comparison of cross sections and analyzing powers calculated by the dispersive OMP with experimental data at 160 and 185 MeV is also presented. The dispersive OMP with a smooth energy dependence is extended to the negative energy region with the guidance of the known first single-particle and single-hole state energies near the Fermi energy, $E_F = -6.8$ MeV, to provide parameters for the shell model potential. This analysis also provides estimates for single-particle and hole energies E_{nlj}, root-mean-square radii R_{nlj}, expectation values of the effective mass $\langle m^*/m \rangle_{nlj}$, occupation probabilities N_{nlj}, absolute spectroscopic factors S_{nlj}, and spectral functions $\zeta_{nlj}(E_x)$ for proton single-particle and single-hole orbits in ^{90}Zr. These estimates are compared with available experimental information.

PACS number(s): 24.10.Ht, 24.70.+s, 25.40.Cm

I. INTRODUCTION

In recent years, dispersive optical model potential (OMP) analysis of elastic nucleon-nucleus scattering data has been recognized as a powerful tool connecting the shell model potential at negative energies with the optical model potential at positive energies [1–5]. The real central term in a dispersive OMP is represented by two components, the so-called Hartree-Fock term, $V_{\rm HF}(E)$, which represents the local equivalent of the nonlocal mean field and is constructed to have a smooth energy dependence over a large energy range that includes the Fermi energy, and a second term, which is evaluated using the dispersion relation connecting the real and imaginary potentials. The second term, called the dispersive correction, has a more complicated energy dependence, especially in the vicinity of the Fermi energy. The Hartree-Fock term is evaluated in the positive energy region using elastic differential cross section and analyzing power data, and then, with the help of the known first single-particle and single-hole state energies near the Fermi energy, it is extrapolated to negative energies. This mean field can then be used to evaluate binding energies of single-particle and single-hole states where there is no experimental data available. It also may be used to evaluate values of the root-mean-square radii, expectation values of the effective mass, occupation probabilities, absolute spectroscopic factors and spectral functions for nucleon single-particle and single-hole orbits.

Dispersive OMP analysis also has been applied to nucleus-nucleus systems [6,7], where the energy dependence of the real central potential at low energies has been studied, and contributions of the dispersion correction terms in the real central potential are evaluated. For a nucleus-nucleus system, the dispersive OMP analysis is limited to the positive energy region, since it is not yet clear how to interpret particle clusters bound in a nucleus.

There are mainly two methods for dispersive OMP analyses reported in the literature. These methods are distinguished by the way in which the constraints of a dispersion relation between the real and imaginary central potentials, and the requirement of a smooth energy dependence of a particular form, are applied to the problem of obtaining dispersive OMP parameters. One, called the iterative moments analysis [3], works with an expansion of the potential in moments weighted by r^n. The coefficients of this expansion, which is based on a more conventional set of single-energy optical model fits to elastic scattering data, are themselves reproduced in a multienergy analysis including Hartree-Fock and dispersive correction terms. In the other method, called the dispersive optical model analysis [2,4,5], the energy-dependent potential parameters are varied to obtain a good fit to the experimental cross sections and analyzing powers in a grid search. Both methods give a reasonable reproduction of experimental data, however, the quality of the dispersive fits is not as good as that of best fits in a conventional OMP analysis. One factor is clearly the smaller number of dispersive OMP parameters coupled with the constraint that they follow a smooth function of

the proton incident energy [2,4,5].

In Ref. [7], we took a different approach in the analysis of deuteron elastic scattering from ^{208}Pb. Constraints of the dispersive analysis are applied to the volume integrals of the potentials, since they are better determined by the data than any single OMP parameter. Initial values of the volume integrals are obtained from best fits obtained by applying a conventional OMP to individual data sets. These volume integrals exhibit a smooth and easily parametrized energy dependence. In the subsequent search using dispersive constraints, the volume integrals of the imaginary terms are kept fixed to the parametrized values. The volume integrals of the correction terms in the real central potential are evaluated using the volume integrals of the imaginary potentials through the dispersion relation (see Sec. II). Then, a dispersive OMP analysis is made in which the geometry and strength parameters are chosen to reproduce these volume integrals, as well as the original measurements.

Dispersive OMP analysis has been applied to the neutron-^{40}Ca [1], -^{51}V [8], -^{86}Kr [9], -^{89}Y [10], -^{90}Zr [5,11], -^{93}Nb [12], -^{113}In [13], -^{208}Pb [2,14], and -^{209}Bi [15] systems, and the proton-^{40}Ca [5] and -^{208}Pb [3,16] systems. Among these nuclei, ^{40}Ca, ^{90}Zr, and ^{208}Pb have been regarded as the nuclei of choice to test the method of dispersive optical model potential analysis. Therefore, a dispersive OMP analysis of the proton-^{90}Zr system is useful. In this paper, we present the best-fit for proton-^{90}Zr elastic scattering data using dispersive OMP and compare it to the best-fit results obtained with conventional OMP analyses. Moreover, the proton-^{90}Zr mean field with a smooth energy dependence is determined from the data sets over a large energy range, and the properties of proton bound states in ^{90}Zr are evaluated.

The proton data used in the dispersive OMP analysis are the cross section and analyzing power data reported at proton energies of 9.8 [17], 20.3 [18], 30.0 [19], 40.0 [20], 49.4 [21], 65.0 [22], 79.8 [23], 100.4 [23], and 135.0 MeV [23]. Data much below the Coulomb barrier ($\sim$10 MeV for ^{90}Zr) or close to the isobaric analog state resonance [24–26] were not included. For the data at E_p=9.8 MeV [17], the analyzing powers have values as large as 0.2 and the compound nucleus contributions at this energy are relatively small [27]; therefore we kept this data in our analysis. At energies above 135 MeV, the volume integral of the imaginary potential shows a significant increase for proton energies above the pion production channel, and these energies were not included in this analysis.

Section II describes the best-fit dispersive OMP analysis. In Sec. III, the proton-^{90}Zr mean field with a smooth energy dependence is presented. In Sec. IV, we present our results for the bound single-particle state energies, effective masses, root-mean-square radii, expectation values of the effective mass, occupation probability, absolute spectroscopic factors and spectral functions. Comparisons are made with available experimental information. In Sec. V, a discussion section, we compare the empirical mean fields from proton-^{40}Ca and -^{208}Pb with the results presented here for ^{90}Zr. Finally, Sec. VI presents a summary of this study.

II. BEST-FIT DISPERSIVE OMP ANALYSIS

The method developed in Ref. [7] for study of the best-fit dispersive OMP analysis is used here. Before evaluating the volume integral of the dispersive correction terms, one needs first to parametrize the volume integral of the imaginary potential obtained in a conventional OMP analysis. The data we use here cover a wide energy range (9.8–135 MeV proton energies) and were taken over the last three decades. Data below 80 MeV were analyzed using non-relativistic treatments [17–22], and at or above 80 MeV were analyzed using a modified *Schrödinger* equation and relativistic kinematics [23]. In order to obtain a consistent parameter set we reanalyzed the entire data set with relativistic kinematics and a conventional OMP. Relativistic kinematics also was used in the dispersive OMP analysis.

The conventional proton-^{90}Zr OMP, $U(r,E)$, is given by

$$U(r,E)=V_C(r)-U_p(r,E)-U_{\rm SO}(r,E) \tag{1}$$

where the $V_C(r)$ is the Coulomb potential and is taken to be that of a charged sphere or radius $R_C=r_C A^{1/3}$. A value of the reduced charge radius r_C=1.235 fm was used [28]. $U_p(r,E)$ is the central part of the proton-^{90}Zr optical potential and $U_{\rm SO}(r,E)$ is the spin-orbit part. The central part is defined as

$$\begin{aligned} U_p(r,E)&=V(r,E)+iW(r,E)\\ &=V_V(E)f(r,R_V,a_V)+iW_S(E)f(r,R_W,a_W)\\ &\quad -i4a_D W_D(E)\frac{d}{dr}f(r,R_W,a_W)\ , \end{aligned} \tag{2}$$

where $f(r,R_j,a_j)$ with $j=V,W$ is a function with a Woods-Saxon form. $W(r,E)$ is the sum of the volume part, $W_S(r,E)$, and the surface part, $W_D(r,E)$. For the spin-orbit part $U_{\rm SO}(r,E)$, the radial dependence is assumed to be that of the Thomas form factor

$$\begin{aligned} U_{\rm SO}(r,E)&=2V_{\rm SO}\frac{1}{r}\frac{d}{dr}f_{\rm SOR}(r,R_{\rm SOR},a_{\rm SOR})\mathbf{l}\cdot\mathbf{s}\\ &\quad +i2W_{\rm SO}\frac{1}{r}\frac{d}{dr}f_{\rm SOI}(r,R_{\rm SOI},a_{\rm SOI})\mathbf{l}\cdot\mathbf{s}\ . \end{aligned} \tag{3}$$

In the reanalysis of the data within the framework of the conventional OMP using relativistic kinematics, we chose ten free parameters, $(V,r_V,a_V,W_S,W_D,r_W,a_W,V_{\rm SO},r_{\rm SOR},a_{\rm SOR})$, which were used for best fits for energies below 50 MeV and an additional three parameters, $(W_{\rm SO},r_{\rm SOI},a_{\rm SOI})$, for energies above 50 MeV. The geometry parameters r_W and a_W were taken to be the same for both the W_S and W_D terms in the imaginary potential. The parameters from this analysis are listed in Table I. The predicted cross sections and analyzing powers using these best-fit parameters are almost identical to the solid line in Figs. 1 and 2, which are the results of the best-fit analysis with the dispersive OMP (discussed later in this section).

In a dispersion relation treatment, the real central potential, $V(r,E)$, consists of a term which varies slowly with energy, the Hartree-Fock (HF) term, $V_{\rm HF}(r,E)$, plus

TABLE I. Best-fit conventional optical model potential parameters. Units are MeV and fm.

E (MeV)	9.8	20.3	30	40	49.35
V	51.62	50.46	57.13	46.97	48.43
r_V	1.274	1.204	1.094	1.176	1.153
a_V	0.621	0.620	0.792	0.690	0.749
W_S			3.43	3.66	8.70
W_D	10.85	8.17	5.80	4.75	2.86
r_W	1.353	1.299	1.331	1.292	1.268
a_W	0.350	0.601	0.666	0.686	0.548
V_{SO}	7.052	5.420	5.959	6.576	6.383
r_{SOR}	0.901	1.026	0.909	1.017	1.074
a_{SOR}	0.365	0.693	0.478	0.872	0.759
W_{SO}					
r_{SOI}					
a_{SOI}					

E (MeV)	65	79.8	100.4	134.8
V	37.03	34.76	29.11	24.74
r_V	1.222	1.198	1.217	1.239
a_V	0.764	0.668	0.691	0.687
W_S	10.32	7.12	8.12	10.36
W_D	1.08			
r_W	1.322	1.446	1.391	1.338
a_W	0.404	0.480	0.546	0.623
V_{SO}	5.625	5.210	4.742	3.734
r_{SOR}	1.140	1.053	1.074	1.056
a_{SOR}	0.702	0.688	0.652	0.605
W_{SO}		−0.729	−0.961	−1.722
r_{SOI}		1.006	0.966	1.050
a_{SOI}		0.306	0.625	0.599

a correction term, $\Delta V(r,E)$, which is calculated using a dispersion relation, so that

$$U_p(r,E)=V_{\rm HF}(r,E)+\Delta V(r,E)+iW(r,E)\ , \tag{4}$$

where

$$\Delta V(r,E)=(E_F-E)\frac{P}{\pi}\int_{-\infty}^{\infty}\frac{W(r,E')}{(E'-E_F)(E-E')}dE'\ . \tag{5}$$

The symbol P denotes the principal value. For the proton-^{90}Zr case, $E_F=-6.8$ MeV and is half the sum of the proton separation energies for ^{90}Zr and ^{91}Nb [29]. The term $\Delta V(r,E)$ is divided into two terms, ΔV_S and ΔV_D, which arise through dispersion relations from the two terms in the imaginary potential, W_S and W_D. Accordingly we rewrite Eq. (2) as

$$\begin{aligned}U_p(r,E)=V(r,E)+iW(r,E)&=V_{HF}(r,E)+\Delta V_S(r,E)+\Delta V_D(r,E)+iW_S(r,E)+iW_D(r,E)\\&=V_{\rm HF}(E)f(r,R_{\rm HF},a_{\rm HF})+\Delta V_S(E)f(r,R_S,a_S)-4a_D\Delta V_D(E)\frac{d}{dr}f(r,R_D,a_D)\\&\quad+iW_S(E)f(r,R_S,a_S)-i4a_DW_D(E)\frac{d}{dr}f(r,R_D,a_D)\ ,\end{aligned} \tag{6}$$

where $f(r,R_j,a_j)$ with $j=\mathrm{HF},S,D$ represents the Woods-Saxon functional dependence. We will make the connection between the imaginary potential and the real correction term though the volume integral per nucleon. The dispersion relation [see Eq. (5)] stated in terms of the volume integral is

$$J_{\Delta V}(E)=(E_F-E)\frac{P}{\pi}\int_{-\infty}^{\infty}\frac{J_W(E')}{(E'-E_F)(E-E')}dE'\ . \tag{7}$$

In this study, the energy dependence of the volume integrals of the best-fit imaginary potentials, $J_W(E)$ and $J_{W_S}(E)$ (shown in Fig. 3), were described using the parametrization [30]

$$J_i(E)=\alpha_i\frac{(E-E_F)^4}{(E-E_F)^4+\beta_i^4}\ , \tag{8}$$

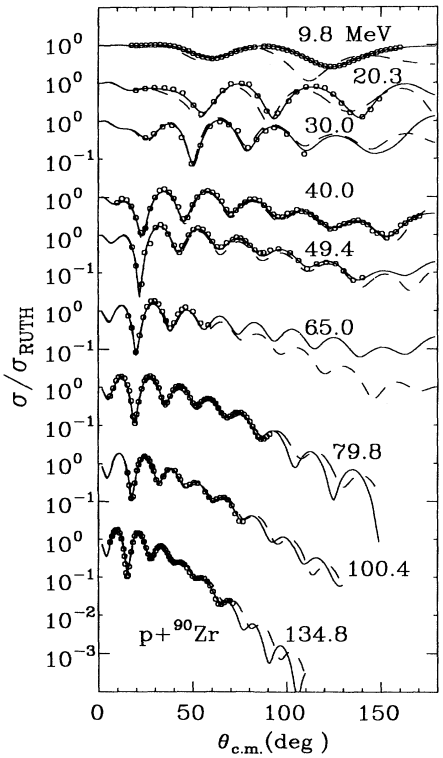

FIG. 1. Angular distributions of the cross section for proton elastic scattering from ^{90}Zr. The circles indicate experimental data. The solid lines are the best-fit results using the dispersive OMP (Table II) and the dashed lines are the calculations using dispersive OMP parameters with a smooth energy dependence.

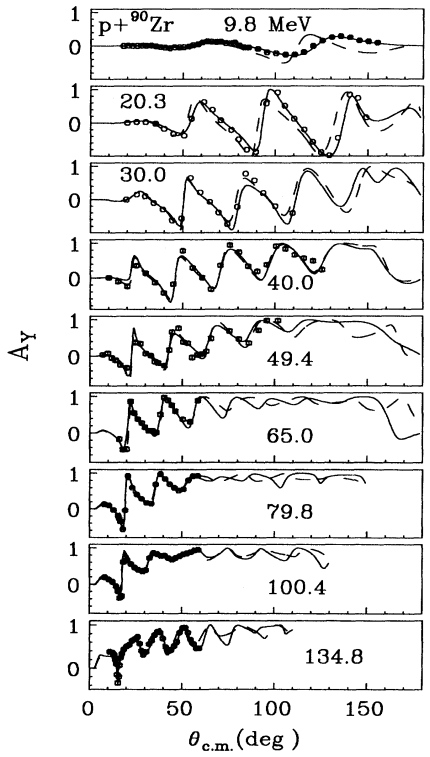

FIG. 2. As in Fig. 1 but for analyzing powers.

where $i=W$ and W_S for the total imaginary potential and the volume part only, respectively. Then, the surface part of the imaginary potential is the difference between the two, $J_{W_D}(E)=J_W(E)=J_{W_S}(E)$. In producing the curves in Fig. 3, we used the following parameter values: $\alpha_W=\alpha_{W_S}=106.97$ MeV fm^3, $\beta_W=12.208$ MeV, and $\beta_{W_S}=46.695$ MeV. Substituting Eq. (8) into Eq. (7), the dispersion correction term can be written in an analytical form [15] as

$$J_{\Delta V}=\frac{\alpha_W\beta_W(E-E_F)[(E-E_F)^2+\beta_W^2]}{\sqrt{2}[(E-E_F)^4+\beta_W^4]} . \tag{9}$$

Also using Eq. (9), one can evaluate the $J_{\Delta V_S}(E)$ by replacing α_W and β_W by α_{W_S} and β_{W_S}, respectively. Then, $J_{\Delta V_D}(E)$ becomes the difference, $J_{\Delta V}-J_{\Delta V_S}$.

Adopting the method used in the best-fit dispersive OMP analysis in Ref. [7], the volume integrals of the imaginary potentials, $J_{W_S}(E)$ and $J_{W_D}(E)$, shown in Fig. 3, and the dispersive correction potentials, $J_{\Delta V_S}(E)$ and $J_{\Delta V_D}(E)$, shown in Fig. 4, were fixed at the values calculated using Eqs. (8) and (9). The geometrical parameters for these potentials were optimized while the depths of these potentials were calculated as follows:

$$\Delta V_S(E)=\frac{J_{\Delta V_S}}{\int f(r,R_S,a_S)d\mathbf{r}} , \tag{10}$$

$$\Delta V_D(E)=\frac{J_{\Delta V_D}}{4a_D\int(d/dr)f(r,R_D,a_D)d\mathbf{r}} , \tag{11}$$

$$W_S(E)=\frac{J_{W_S}}{\int f(r,R_S,a_S)d\mathbf{r}} , \tag{12}$$

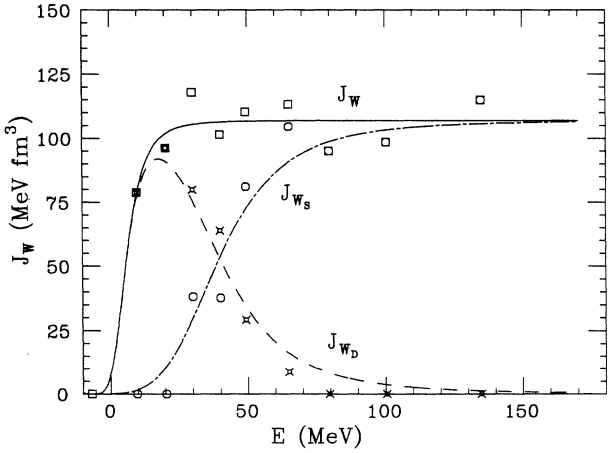

FIG. 3. Energy dependence of the volume integrals of the imaginary central optical potentials for proton elastic scattering from ^{90}Zr. The square, circle, and crosses with holes refer to $J_W(E)$, $J_{W_S}(E)$, and $J_{W_D}(E)$, respectively, from best-fit conventional OMP analysis. The analytic parametrizations of the energy dependence of $J_W(E)$, $J_{W_D}(E)$, and $J_{W_S}(E)$ are shown by the solid, dash and dot-dashed lines.

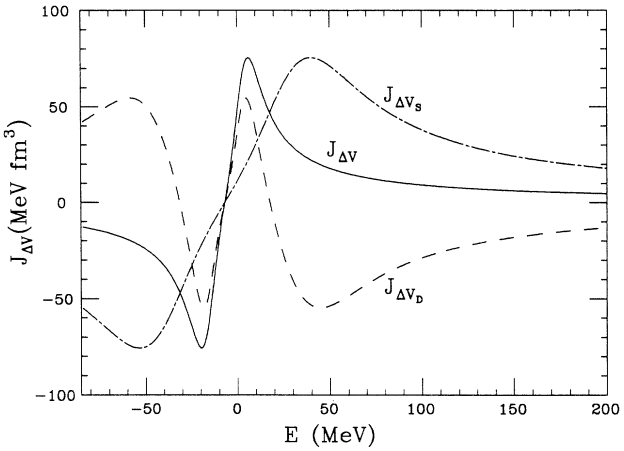

FIG. 4. Energy dependence of the volume integrals of the dispersive corrections terms. The solid line is the total correction term, $J_{\Delta V}(E)$. The dot-dashed line refers the volume correction term, $J_{\Delta V_S}(E)$ and the dashed line represents the surface correction term, $J_{\Delta V_D}(E)$.

and

$$W_D(E)=\frac{J_{W_D}}{4a_D\int(d/dr)f(r,R_D,a_D)d\mathbf{r}} . \quad (13)$$

The other parameters, including the real central and spin-orbit depths as well as the radial shape of the imaginary potential, were allowed to vary. This gave ten adjustable parameters ($V_{\rm HF}$,$r_{\rm HF}$,$a_{\rm HF}$,r_S,a_S,r_D,a_D,$V_{\rm SO}$, $r_{\rm SOR}$,$a_{\rm SOR}$), the same number as the conventional OMP (V,r_V,a_V,W_S,W_D,R_W,a_W,$V_{\rm SO}$,$r_{\rm SOR}$,$a_{\rm SOR}$), for energies below 50 MeV and three additional imaginary spin-orbit potential parameters for data energies above 50 MeV in both the conventional and the dispersive OMP analyses. Despite the similarity in the number of adjustable parameters, the dispersive optical model brings additional physical constraints to the description of the elastic scattering, resulting in a more self-consistent model.

In order to carry out the analysis, the computer code SNOOPY8Q [31] was modified [32] to include the form of the central part of the dispersive optical potential $U_p(r,E)$ as defined in Eq. (6). The individual best-fit parameters in this dispersive analysis were obtained when the minimum total chi squared, $\chi^2_{\rm tot}$, was achieved for the difference between the cross section and analyzing power data and their calculated values. Results of the best-fit dispersive OMP analysis are shown in Fig. 1 and 2 as solid lines. Best-fit dispersive OMP parameters are shown in Table II. The calculations with best-fit conventional OMP parameters gave very similar fits and are not plotted, since differences would not be seen in the scale of the plots (Figs. 1 and 2). The similar quality of fit demonstrates that a dispersive OMP analysis is as successful in reproducing measurements both globally and at single energies as a conventional OMP analysis. The ratio of the total χ^2 of the best-fit dispersive and conventional OMP analyses are shown in Fig. 5 as a function of energy.

TABLE II. Best-fit dispersive optical model potential parameters. Units are MeV and fm.

E (MeV)	9.8	20.3	30	40	49.35
$V_{\rm HF}$	51.45	45.77	44.80	44.37	38.40
$r_{\rm HF}$	1.182	1.209	1.217	1.166	1.233
$a_{\rm HF}$	0.671	0.627	0.598	0.821	0.755
r_S	1.170	1.324	1.381	1.343	1.307
a_S	0.731	0.775	0.747	0.614	0.506
r_D	1.337	1.319	1.142	1.308	1.222
a_D	0.342	0.499	0.829	0.663	0.663
$V_{\rm SO}$	5.864	5.392	4.795	7.094	5.719
$r_{\rm SOR}$	0.873	1.086	0.961	0.994	1.065
$a_{\rm SOR}$	0.51	0.58	0.33	0.88	0.74
$W_{\rm SO}$					
$r_{\rm SOI}$					
$a_{\rm SOI}$					

E (MeV)	65	79.8	100.4	134.8
$V_{\rm HF}$	30.32	33.66	28.50	20.90
$r_{\rm HF}$	1.254	1.179	1.156	1.279
$a_{\rm HF}$	0.841	0.742	0.797	0.719
r_S	1.270	1.392	1.361	1.331
a_S	1.022	0.534	0.552	0.586
r_D	1.505	1.293	1.474	1.305
a_D	0.511	0.819	1.129	0.795
$V_{\rm SO}$	4.559	5.817	5.214	4.061
$r_{\rm SOR}$	1.076	1.042	1.065	1.059
$a_{\rm SOR}$	0.62	0.71	0.69	0.64
$W_{\rm SO}$	−0.576	−1.076	−0.848	−1.344
$r_{\rm SOI}$	1.199	0.983	0.993	1.020
$a_{\rm SOI}$	0.34	0.33	0.65	0.59

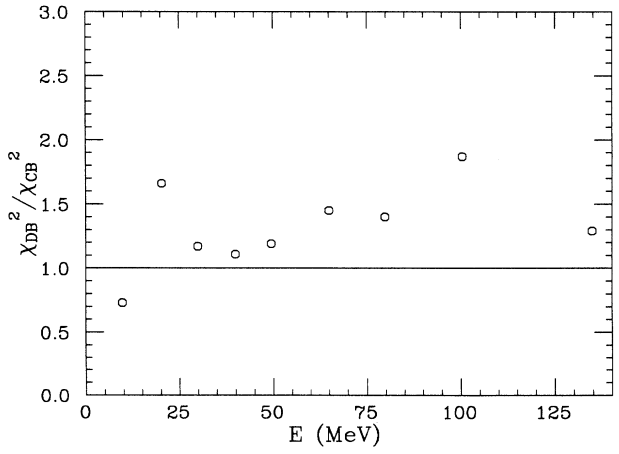

FIG. 5. Total chi-squared ratios, $\chi^2_{\rm DB}/\chi^2_{\rm CB}$. The symbols DB and CB stand for the dispersive OMP best fit and the conventional OMP best fit, respectively.

Values larger than one reflect the fact that there are additional constraints in the dispersive OMP.

III. PROTON-^{90}Zr MEAN FIELD WITH A SMOOTH ENERGY DEPENDENCE

The properties of the proton-^{90}Zr mean field with fixed geometrical parameters and potential depths which vary smoothly with energy are presented in this section. In the process of determining this mean field, through a grid search, the volume integrals of the imaginary potential and the dispersive correction potentials were fixed at the values calculated from Eqs. (8) and (9). The r_{W_S}, a_{W_S} are not constrained in the present work as in previous work [1–5], in which r_{W_S} and a_{W_S} were set equal to $r_{\rm HF}$ and $a_{\rm HF}$, respectively. This was necessary to obtain a reasonable overall fit to the cross section and analyzing power data, which covers the energy range from 9.8 to 135 MeV. The modified code SNOOPY8Q [32] treats separately the HF potential and the volume part of the dispersive correction potential, which makes this treatment feasible.

The radius and diffuseness of the imaginary volume part $W_S(r,E)$ are determined mainly from data with energies higher than 80 MeV, where the imaginary surface potential is negligible. Then the form factor of the imaginary surface potential $W_D(r,E)$ is determined mainly from data with $E_p \leq 80$ MeV. Fitting to the entire data set using the potentials defined in Eqs. (6) and (3), the following potential form factors were obtained: (i) the HF potential,

$$r_{\rm HF}=1.217 \text{ fm} \quad \text{and} \quad a_{\rm HF}=0.76 \text{ fm} ; \tag{14a}$$

(ii) the volume imaginary and dispersive correction potentials,

$$r_{W_S}=1.37 \text{ fm} \quad \text{and} \quad a_{W_S}=0.588 \text{ fm} ; \tag{14b}$$

(iii) the surface imaginary and dispersive correction potentials,

$$r_{W_D}=1.294 \text{ fm} \quad \text{and} \quad a_{W_D}=0.607 \text{ fm} ; \tag{14c}$$

(iv) spin-orbit potentials,

$$r_{\rm SOR}=r_{\rm SOI}=1.05 \text{ fm} \quad \text{and} \quad a_{\rm SOR}=a_{\rm SOI}=0.6 \text{ fm} . \tag{14d}$$

The depth $V_{\rm SO}(E)$ of the real spin-orbit potential was found to be

$$V_{\rm SO}(E)=6.0-0.0178E \text{ (MeV)} . \tag{15a}$$

A small negative imaginary spin-orbit potential was necessary to give a good fit to the analyzing power data for energies above 50 MeV:

$$\begin{aligned} W_{\rm SO}(E)&=0 , \quad E \leq 50 \text{ MeV} , \\ &=-0.0175(E-50) , \quad E \geq 50 \text{ MeV} . \end{aligned} \tag{15b}$$

The depth $V_{\rm HF}$ of the HF potential is determined from fits of the individual data sets at each energy after the form factors and other potential components have been fixed at the values given in Eqs. (9)–(15). The $V_{\rm HF}$ are shown as open circles at positive energies in Fig. 6. In order to obtain reliable bound-state information, $V_{\rm HF}(E)$ was also constrained to reproduce the potential depths needed for the closest particle and hole states near the Fermi energy. The smooth curve, described in the next section, is also shown in Fig. 6.

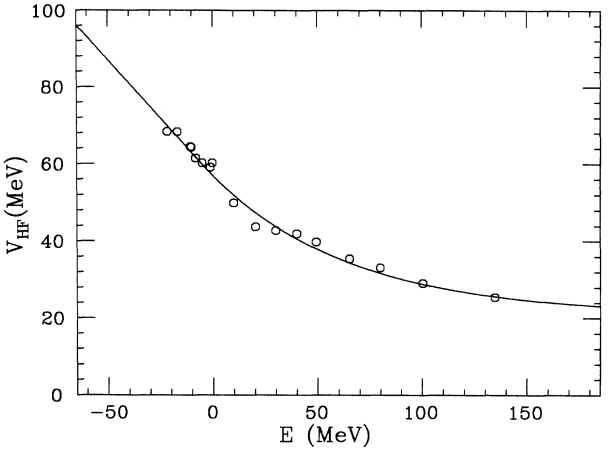

FIG. 6. Energy dependence of the HF potential depth $V_{\rm HF}(E)$. The circles at negative energies are the best-fit to the experimental single-particle energies E_{nlj} when the values of the $\Delta V(r,E_{nlj})$ are used. The circles at positive energies are the best-fit to the scattering data. The solid line refers to the HF potential depth $V_{\rm HF}$ given in Eqs. (16) and (17).

The calculated cross sections and analyzing powers using the dispersive OMP parameters [Eqs. (8) to (16)] are shown as dashed lines in Figs. 1 and 2. As can be seen, good agreement between the data and calculations is

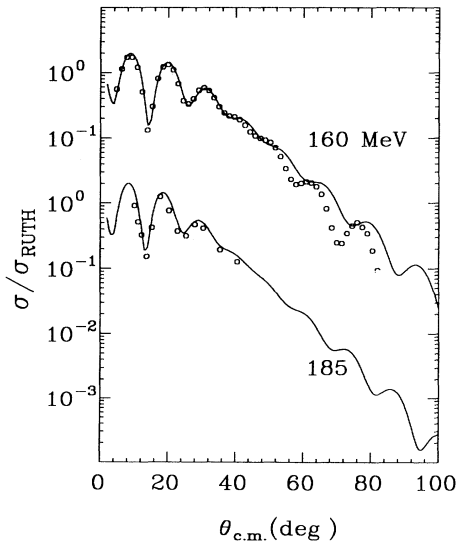

FIG. 7. Angular distributions of the cross section for proton elastic scattering from ^{90}Zr at 160 and 185 MeV. The circles indicate experimental data. The calculations using dispersive OMP parameters with a smooth energy dependence are shown as solid lines.

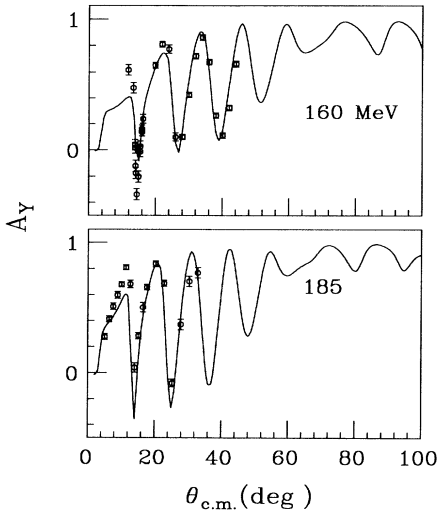

FIG. 8. As in Fig. 7 but for analyzing powers.

achieved, except for the data set at $E_p = 9.8$ MeV. Moreover, the comparison between the data and calculations at higher energies from extrapolation of the dispersive OMP parameters with smooth energy dependence to 160 [23], and 185 [23,33] MeV is shown in Figs. 7 and 8, and the agreement is reasonable. The dispersive and conventional OMP parameters have also been used to predict reaction cross sections σ_R. The comparison between data [34] and the calculations is shown in Fig. 9. Reaction cross sections, $\sigma_R(E)$, calculated with dispersive OMP parameters with smooth energy dependence overestimate the data at low energies and underestimate it at high energies.

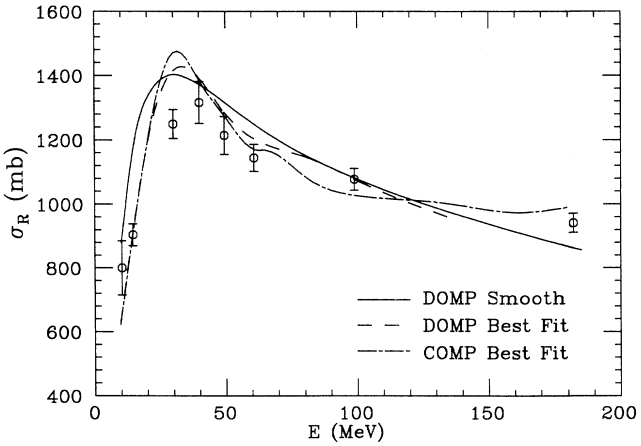

FIG. 9. Reaction cross sections, $\sigma_R(E)$. The circles are experimental data and the solid line is the calculation using dispersive OMP parameters with a smooth energy dependence (DOMP Smooth). The σ_R calculated using dispersive OMP best-fit (DOMP best fit) and conventional OMP best-fit (COMP best fit) parameters are shown by the dashed and dot-dashed lines, respectively.

IV. BOUND STATE PROPERTIES

An appealing feature of the dispersive OMP analysis is that it provides the shell model potential for bound states from the extrapolation of the dispersive OMP to negative energies. A wealth of experimental information is available for the single-particle and single-hole energies for these orbits near the Fermi energy in ^{90}Zr. The spectroscopic information on these orbits in ^{90}Zr has been measured by various means, such as stripping and pickup reactions, and $(e,e'p)$ (see Ref. [35]). Experimental centroid energies and sums of the spectroscopic factors for the subshells in ^{90}Zr are discussed below and tabulated for comparison with the results of the present work in Tables III and IV, respectively. The general appearance of the measured proton bound state properties in ^{90}Zr is that the centroid energies for a given subshell measured by different reactions are in a good agreement. However, there are large discrepancies for the spectroscopic factors obtained from $(e,e'p)$ reported in Ref. [35], with $(d,^3\mathrm{He})$ reported in Ref. [36], and with (n,d) reported in Ref. [37] for the subshells below the Fermi energy. Also there are sizable differences for spectroscopic factors measured by (d,n) and $(^3\mathrm{He},d)$ reactions [38,39] for the orbits above the Fermi energy, except for the $1g_{9/2}$ orbit. A detail development of these points is given in the following subsections.

A. Single-particle energies

Single-particle energy (E_{nlj}) calculations are performed using a subroutine implemented in the distorted wave code DWUCK4 [40] that solves the *Schrödinger* equation

$$\left[-\frac{\nabla^2}{2m}+V(r,E_{nlj})\right]\Phi_{nlj}(\mathbf{r})=E_{nlj}\Phi_{nlj}(\mathbf{r}) ,$$

where the $V(r,E_{nlj})$ is the real part of the dispersive OMP, which is the sum of the HF, $\Delta V_S(r,E)$, and $\Delta V_D(r,E)$ potentials. Also included is the spin-orbit potential. We adopted the similar treatment for the spin-orbit potential depth as in Ref. [4], the depth, $V_{SO}(E)=V_{SO}(0)=6.0$ MeV, was used in the calculation of the single-particle energies for all proton bound states. The single-particle wave function for a subshell with the quantum number nlj can be written as

$$\Phi_{nlj}(\mathbf{r})=\frac{u_{nlj}(r)}{r}Y_{lm}(\Omega) .$$

Based on the existing experimental information for first single particle and hole states near the Fermi energy, which is shown in Table III, the depth V_{HF} was adjusted to reproduce the bound state energies. The dispersive correction terms, ΔV_S and ΔV_D, were included in the potential and fixed at the values calculated using Eq. (9). At the Fermi energy the value of the potential depth is $V_{HF}=60.8$ MeV.

The energy dependence of V_{HF} has been described before using an exponential as function of energy [2]. With this form a reasonable reproduction of the positive energy values can be obtained, but the extrapolation to nega-

TABLE III. Energy of proton single-particle orbits in ^{90}Zr. The numbers in parentheses are the experimental uncertainties in E_{nlj}.

		E_{nlj} (MeV)				
nlj	Present work	$(e,e'p)$ Ref. [35]	$(d,^3\text{He})$ Ref. [36]	(n,d) Ref. [37]	$(^3\text{He},d)$ Ref. [39]	(d,n) Ref. [38]
$2d_{5/2}$	−0.45				−1.30	−1.09
$1g_{7/2}$	[a]				−0.34	
$1g_{9/2}$	−4.87				−5.11	−5.16
$2p_{1/2}$	−8.60	−8.36	−8.36	−8.36		
$2p_{3/2}$	−10.30	−10.4(2)	−9.87	−9.87		
$1f_{5/2}$	−9.68	−10.8(2)	−10.11	−10.11		
$1f_{7/2}$	−15.69	−17.0(5)	−15.56			
$2s_{1/2}$	−24.01	−21.8(4)				
$1d_{3/2}$	−25.19	−23.8(5)[b]				
$1d_{5/2}$	−30.39					
$1p_{1/2}$	−41.81					
$1p_{3/2}$	−44.40					
$1s_{1/2}$	−59.88					

[a] E_{nlj} was found larger than zero.
[b] Average value for the orbits noted by (nl), for example, the average value of the single-particle energy for $1d_{3/2}$ and $1d_{5/2}$ is −23.8(5) MeV.

tive energies underestimates the potential depths required by the bound state energies. To increase the energy dependence near $E=0$, a constant term was added, giving

$$V_{\text{HF}}(E)=V_{\text{HF}}^{(1)}(E_F) + V_{\text{HF}}^{(2)}(E_F)\exp\left[\frac{-\lambda(E-E_F)}{V_{\text{HF}}^{(2)}(E_F)}\right], \quad E>E_F . \tag{16}$$

The sum of $V_{\text{HF}}^{(1)}(E_F)+V_{\text{HF}}^{(2)}(E_F)$ was fixed at 60.8 MeV to match at the Fermi energy, and the individual coefficients adjusted to reproduce the positive energy values of V_{HF} [producing $V_{\text{HF}}^{(1)}(E_F)=21.0$ MeV, $V_{\text{HF}}^{(2)}(E_F)=39.8$ MeV, and $\lambda=0.606$].

Unfortunately, this parametrization tends to overestimate the values of V_{HF} below the Fermi energy, so in this region V_{HF} is parametrized with a linear function

$$V_{\text{HF}}(E)=V_{\text{HF}}(E_F)-\lambda(E-E_F), \quad E<E_F . \tag{17}$$

The single-particle energies were recalculated, holding $V_{\text{HF}}(E)$ at the values given by the smooth parametrization. The values calculated using only the $V_{\text{HF}}(r,E)$ term of the potential are shown in the first column of Fig. 10, while in the second column the values are shown, which are calculated including the additional dispersive correction term, $V_{\text{HF}}(r,E)+\Delta V(r,E)$. These bound state energies are also tabulated in the first column of Table III. In

TABLE IV. Spectroscopic factors of the proton single-particle orbits in ^{90}Zr. The numbers in parentheses are the experimental uncertainties in S_{nlj}.

		S_{nlj} (MeV)				
nlj	Present work	$(e,e'p)$ Ref. [35]	$(d,^3\text{He})$ Ref. [36]	(n,d) Ref. [37]	$(^3\text{He},d)$ Ref. [39]	(d,n) Ref. [38]
$2d_{5/2}$	0.682				0.83	0.435
$1g_{7/2}$					0.38	
$1g_{9/2}$	0.666				1.0	0.97
$2p_{1/2}$	0.680	0.36(4)	0.90	0.85(3)		
$2p_{3/2}$	0.660	0.56(6)	0.98	0.45(13)		
$1f_{5/2}$	0.665	0.60(8)	1.48	0.13(7)		
$1f_{7/2}$	0.670	0.68(9)	1.41			
$2s_{1/2}$	0.959	0.64(8)				
$1d_{3/2}$	0.896	0.71(10)[a]				
$1d_{5/2}$	0.876					
$1p_{1/2}$	0.833					
$1p_{3/2}$	0.870					
$1s_{1/2}$	1.114					

[a] Average value for the orbits noted by (nl).

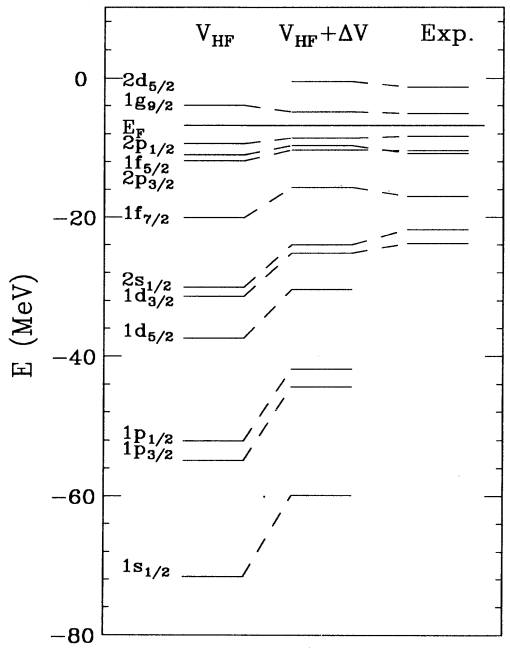

FIG. 10. Single-particle and hole state energies in ^{90}Zr. The experimental values are those obtained from $(e,e'p)$ reactions.

the last column in Fig. 10 are the bound state energies measured in the $(e,e'p)$ reaction [35]. Compared with our calculation, the nuclear dynamics compress the single-particle levels around the Fermi energy. This feature has been observed in previous studies [1–5]. The calculated bound state energies compare well with available experimental data.

B. Other bound-state properties

1. *Effective masses*

Effective masses are important quantities in later calculations for root-mean-square radii, occupation probabilities, spectroscopic factors and spectral functions. The ratio of the total effective mass, m^*, of a proton in a nuclear real central potential to its free mass m, can be written as [3]

$$m^*(r,E)/m = 1 - \frac{d}{dE} V(r,E) \ . \tag{18}$$

The effective mass associated with the HF potential $m^*_{\rm HF}$ is,

$$m^*_{\rm HF}(r,E)/m = 1 - \frac{d}{dE} V_{\rm HF}(r,E) \tag{19}$$

and the ratio of m^* to $m^*_{\rm HF}$, which is called the E mass, is defined as

$$\overline{m}(r,E)/m = m^*/m^*_{\rm HF} = 1 - [m/m^*_{\rm HF}] \frac{d}{dE} \Delta V(r,E) \ . \tag{20}$$

The radial dependence of the three effective masses at $E = E_F$ are shown in Fig. 11.

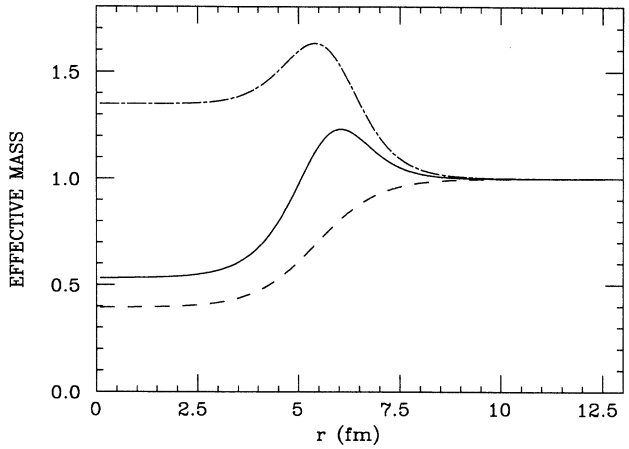

FIG. 11. Radial dependence of the effective masses at $E = E_F$. The solid line is the total effective mass m^*/m, and the dashed line refers to the HF effective mass $m^*_{\rm HF}/m$. The dot-dashed line is the E mass, $m^*/m^*_{\rm HF}$.

In order to take the effect of nonlocality into account, Mahaux and Sartor suggested [3] that the wave function $u_{nlj}(r)$ for $E \leq 0$ should be scaled by the Perey factor $P_{nlj}(r)$. Then the modified wave function noted as $\overline{u}_{nlj}$ is

$$\overline{u}_{nlj}(r) = C_{nlj} P_{nlj}(r) u_{nlj}(r) \ , \tag{21}$$

where

$$P_{nlj}(r) = [m^*_{\rm HF}(r,E_{nlj})/m]^{1/2} \tag{22}$$

and the value C_{nlj} is the normalization factor, which satisfies the relation

$$\int_0^\infty \overline{u}^2_{nlj}(r) dr = 1 \ . \tag{23}$$

TABLE V. Root-mean-square radii, R_{nlj}, of proton single-particle orbits in ^{90}Zr. The numbers in parentheses are the available experimental uncertainties. Also listed are the expectation values of the effective mass ratio $\langle m^*/m \rangle_{nlj}$ for these proton single-particle orbits.

nlj	$R^{\rm rms}_{nlj}$ (fm) Present work	$R^{\rm rms}_{nlj}$ (fm) $(e,e'p)$ Ref. [35]	Theory[a]	$\langle m^*/m \rangle_{nlj}$ Present work
$2d_{5/2}$	5.63			1.10
$1g_{9/2}$	5.01	4.97(10)	4.93	0.947
$2p_{1/2}$	4.77	4.57(9)	4.63	0.902
$2p_{3/2}$	4.66	4.48(7)	4.57	0.917
$1f_{5/2}$	4.51	4.54(7)	4.52	0.841
$1f_{7/2}$	4.39	4.51(11)	4.52	0.814
$2s_{1/2}$	3.90	3.87	3.91	0.543
$1d_{3/2}$	3.90	3.99(10)[b]	4.08	0.554
$1d_{5/2}$	3.99		4.01	0.571
$1p_{1/2}$	3.46			0.544
$1p_{3/2}$	3.53			0.525
$1s_{1/2}$	2.86			0.384

[a]The theoretical calculations [41] given in Table 11 in Ref. [35].
[b]Average value for the orbits noted by (nl).

The modified wave functions $\bar{u}_{nlj}(r)$ are used in the later calculations.

2. Root-mean-square radii

The root-mean square radii are defined as

$$R_{nlj}^{\mathrm{rms}} = \left[\int_0^\infty \bar{u}_{nlj}^2(r) r^2 dr \right]^{1/2} . \tag{24}$$

The calculated root-mean-square radii are listed in Table V and compared with the experimental values obtained from the $(e,e'p)$ reaction [35], and theoretical calculations [41] given in Table 11 of Ref. [35].

3. Occupation probability

Occupation probabilities for the single-particle orbits in which, $E_{nlj} < E_F$ are

$$N_{nlj} = \int_0^\infty \bar{u}_{nlj}^2(r) \left[1 + [m^*_{\mathrm{HF}}/m(r,E_{nlj})]^{-1} \pi^{-1} \int_{E_F}^\infty \frac{W(r,E')}{(E'-E_{nlj})^2} dE' \right] dr , \tag{25}$$

and for $E_{nlj} > E_F$ are

$$N_{nlj} = -\int_0^\infty \bar{u}_{nlj}^2(r) \left[[m^*_{\mathrm{HF}}/m(r,E_{nlj})]^{-1} \pi^{-1} \int_{-\infty}^{E_F} \frac{W(r,E')}{(E'-E_{nlj})^2} dE' \right] dr . \tag{26}$$

The calculated N_{nlj} are listed in Table VI, and compared with the theoretical calculations in Ref. [42].

The occupation probabilities of each orbital (nlj) are also shown as circles in Fig. 12. By drawing continuous curves through the N_{nlj}'s separately at $E < E_F$ and $E > E_F$ and extrapolating these curves to $E = E_F$, the magnitude of the discontinuity, Z, at $E = E_F$ is $Z = 0.53$.

4. Spectroscopic factors

The spectroscopic factor is defined as [3]

$$S_{nlj} = \int_0^\infty \bar{u}_{nlj}^2(r) [m/\bar{m}(r,E_{nlj})] dr , \tag{27}$$

where the $\bar{m}/m(r,E_{nlj})$ is Eq. (20) evaluated at E_{nlj}.

Our S_{nlj} values calculated for bound single-particle and hole states in ^{90}Zr are listed in Table IV. These values should be compared with experimental absolute spectroscopic factors which, in principle, can be obtained from $(e,e'p)$ measurements [35] or through nucleon transfer reactions, such as $(d,{}^3\mathrm{He})$ [36], (n,d) [37] , $({}^3\mathrm{He},d)$ [39], and (d,n) [38] reactions. The experimental S_{nlj} for single-particle states in ^{90}Zr obtained from stripping reactions and for single-hole states obtained from $(e,e'p)$ measurements and pick-up reactions are also listed in Table IV. Comparing the measured S_{nlj} from these different approaches, one notes that there are large discrepancies which may arise from uncertainties in the extraction of this information from experiments. The calculated S_{nlj} in our analysis for single-hole states agree better with the results of the $(e,e'p)$ measurements.

TABLE VI. Occupation probabilities for proton single-particle orbits in ^{90}Zr.

nlj	N_{nlj} (fm) Present work	Theory Ref. [42]
$2d_{5/2}$	0.131	0.054
$1g_{7/2}$		0.04
$1g_{9/2}$	0.210	0.08
$2p_{1/2}$	0.790	0.86
$2p_{3/2}$	0.813	0.88
$1f_{5/2}$	0.804	0.90
$1f_{7/2}$	0.845	0.93
$2s_{1/2}$	0.880	0.96
$1d_{3/2}$	0.880	0.95
$1d_{5/2}$	0.891	0.96
$1p_{1/2}$	0.910	0.97
$1p_{3/2}$	0.913	0.97
$1s_{1/2}$	0.928	0.98

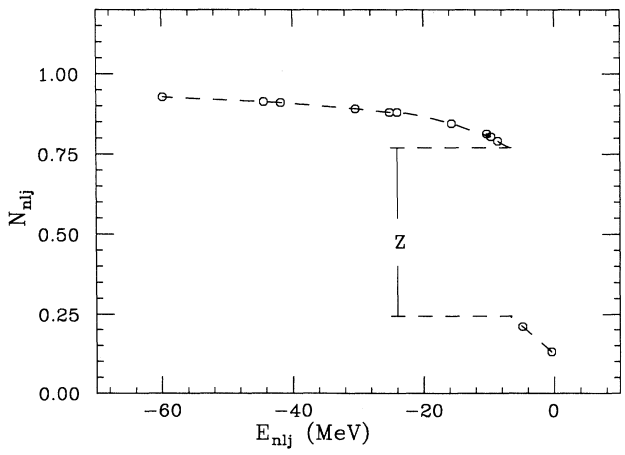

FIG. 12. Values for the occupation probability N_{nlj} vs single-particle energies. The circles are the N_{nlj} shown in Table VI. The dashed lines are guides to the eye. $Z = 0.53$ measures the gap between the two dashed lines at the Fermi energy, $E_F = -6.8$ MeV.

5. *Spectral functions*

The spectral function for a single-particle state nlj is defined as

$$\zeta_{nlj}(E)=-\pi^{-1}\frac{S_{nlj}\langle W_{nlj}(E)\rangle/\langle m^*_{nlj}/m\rangle}{(E-E_{nlj})^2+[\langle W_{nlj}(E)\rangle/\langle m^*_{nlj}/m\rangle]^2}\ , \tag{28}$$

where S_{nlj} represents the absolute spectroscopic factor and $\langle m^*_{nlj}/m\rangle$ is the expectation value of the effective mass m^*/m averaged over the bound state wave function

$$\langle m^*_{nlj}/m\rangle=\int_0^\infty [m^*(r,E_{nlj})/m]\bar{u}^2_{nlj}dr\ . \tag{29}$$

The quantities, $\langle m^*/m\rangle_{nlj}$, have been listed in Table V. The symbol $\langle W_{nlj}(E)\rangle$ denotes the expectation value of the imaginary part of the mean field,

$$\langle W_{nlj}(E)\rangle=\int_0^\infty W(r,E)\bar{u}^2_{nlj}dr\ . \tag{30}$$

Spectral functions calculated for $1f_{7/2}$, $2s_{1/2}$, $1d_{3/2}$, and $1d_{5/2}$ proton hole states in ^{90}Zr are shown in Fig. 13. The individual spectral functions in Fig. 13 are multiplied by $2j+1$, and the spectral function for $1d_{3/2+5/2}$ is the sum of the $1d_{3/2}$ and $1d_{5/2}$ states weighted by $(2j+1)$. These calculated spectral functions are compared with the results from the $(e,e'p)$ experiment [35], which are shown as histograms in Fig. 13. Spectral functions calculated for the $1f_{5/2}$ state and less bound states in ^{90}Zr are δ functions and are not shown. There is no data available from $(e,e'p)$ experiments or nuclear transfer reaction measurements for excitation energies above 21 MeV. The calculated spectral function for the $1f_{7/2}$ proton hole state is in good agreement with the experimental results from $(e,e'p)$ [35]. Predicted strengths for proton hole states, such as the $1d_{3/2+5/2}$ and $2s_{1/2}$ states are located in part at higher excitation energies than the experimental observations, and additional data are needed to give a more meaningful comparison.

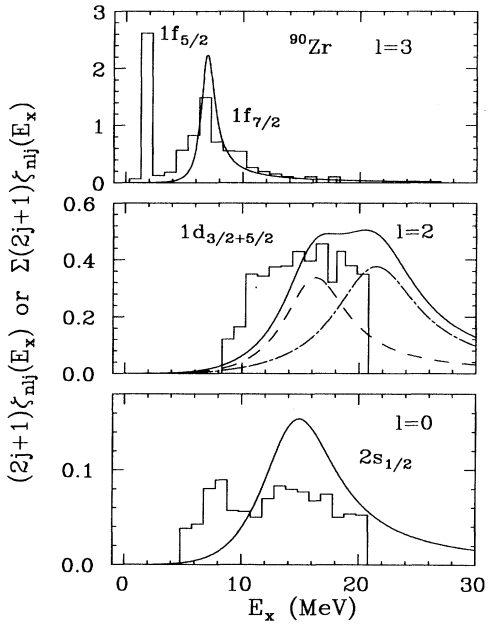

FIG. 13. Spectral functions $\zeta_{nlj}(E_x)$. The histogram is the experimental data from the $(e,e'p)$ reaction [35]. In the top part, the solid line is the calculation for the $1f_{7/2}$ state. In the middle part, the solid line represents the sum of the spectral functions for $1d_{3/2}$ and $1d_{5/2}$ states. The dashed and dot-dashed lines refer to the spectral functions for the $1d_{3/2}$ and $1d_{5/2}$ states, respectively. The solid line in the bottom part is for the $2s_{1/2}$ state.

C. Comparison among ^{90}Zr, ^{40}Ca, and ^{208}Pb

It is interesting to compare some of the proton bound state properties obtained from dispersion analysis for ^{40}Ca [5], ^{90}Zr (present work), and ^{208}Pb [3]. These three spherical nuclei are widely considered as good test cases for nuclear structure studies. The most striking feature, which comes from the comparison is that the surface of the Fermi sea becomes less sharp with increasing mass. The occupation probabilities N_{nlj} for the states just above and below the Fermi sea are 0.14 ($1f_{7/2}$) and 0.85 ($1d_{3/2}$) in ^{40}Ca [5]; 0.210 ($1g_{9/2}$) and 0.79 ($2p_{1/2}$) in ^{90}Zr (present work); and 0.26 ($1h_{9/2}$), and 0.77 ($3s_{1/2}$) in ^{208}Pb [3].

V. DISCUSSION

A. Mean field for proton-^{90}Zr

The volume integral or zeroth moment,

$$J_V/A=\frac{4\pi}{A}\int r^2V(r,E)dr\ ,$$

and the rms radius $R_{\rm rms}=\langle r^2_V\rangle^{1/2}$ or the normalized second moment of the radial distribution:

$$\langle r^2_V\rangle=\frac{\int r^4V(r,E)dr}{\int r^2V(r,E)dr}\ ,$$

of the real part of the mean field are shown as solid lines in Fig. 14. These two real moments of the mean field could be identified with the moments of an equivalent Woods-Saxon potential, with geometrical parameters $\tilde{r}_V$ and $\tilde{a}_V$. By making the assumption that the $\tilde{a}_V=a_V=0.76$ fm (a_V is the diffuseness of the HF potential), $\tilde{r}_V$ is calculated and shown as a solid line in the lower part of Fig. 14 as a function of energy. In the same figure, the dashed lines are the values of the HF potential. The circles are from the best fit of the dispersive OMP to the scattering data at positive energies and to the single-particle energies E_{nlj} at negative energies; the crosses are from the best-fit from the conventional OMP to the scattering data at positive energies. As one can see, the general trend of the best-fit results over all energies can be described by the mean-field potential represented by the solid lines. This level of agreement may result in part from the fact that the same mean-field geometrical parameters are used at all negative energies and that the

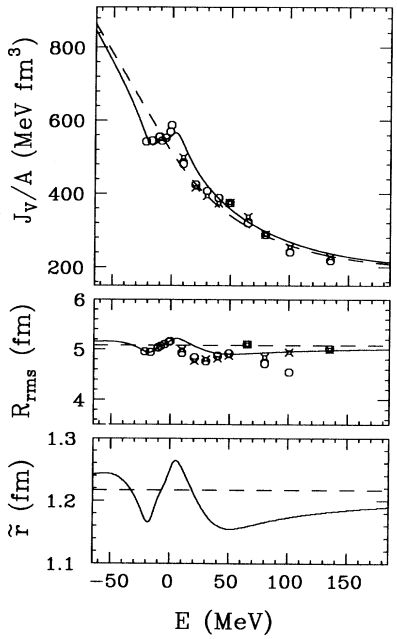

FIG. 14. The energy dependence of the volume integral of the real central dispersive OMP is in the top part of this figure. The circles are the best-fit of the dispersive OMP to the scattering data at positive energies, and to the single-particle energies E_{nlj} at negative energies. The crosses are the best fit from conventional OMP to the scattering data at positive energies. The solid line represents the calculation by the dispersive OMP with a smooth energy dependence. The middle part shows the root-mean-square radii and the bottom part the effective radius. The dashed lines are the values from the HF potential.

only deviation in the mean field is that of the HF. It should be noted that, in the positive energy region, r_V and a_V were allowed to vary to give the best-fit to scattering data.

B. Comparison between empirical mean fields

In this section we briefly compare our results for the proton-^{90}Zr mean field with the proton-^{40}Ca [5], and proton-^{208}Pb [3] empirical mean fields obtained from a dispersive OMP analysis. A comparison of the neutron mean fields for these three nuclei has been made in Ref. [4].

The mean field deduced in these analyses consists of a dispersive contribution due to the coupling of the proton to the excited states of the core added to a smoothly varying energy dependent term $V_{\rm HF}(r,E)$. By definition the latter component is not much influenced by the coupling of the proton to core excitations and, thus, should depend smoothly on mass number A and neutron excess. Woods-Saxon geometrical parameters for these HF potentials are listed in Table VII. HF geometrical parameters for the neutron mean field are listed for comparison. A small increase in the radius parameters $r_{\rm HF}$ with mass number appears to be present. We made an attempt to study the isovector part of the HF potential by comparing the HF potentials obtained from the dispersive OMP analyses for neutron and proton mean fields (Refs. [1–5] and present work), but no conclusive result was obtained. It should be pointed out that the HF potentials for proton-^{40}Ca [5] and proton-^{90}Zr (present work) are obtained from the fits to experimental data up to about 200 MeV and the proton-^{208}Pb [3] is deduced from the fits to experimental data below 60 MeV.

TABLE VII. Geometrical parameters for HF potentials. All values are in fm. A Woods-Saxon radial form has been assumed.

	Proton		Neutron	
	$r_{\rm HF}$	$a_{\rm HF}$	$r_{\rm HF}$	$a_{\rm HF}$
^{40}Ca	1.20[a]	0.73[a]	1.18[b]	0.70[b]
^{90}Zr	1.217	0.76	1.21[c]	0.65[c]
^{208}Pb	1.225[d]	0.71[d]	1.24[e]	0.68[e]

[a]Reference [5].
[b]Reference [1].
[c]Reference [4].
[d]Reference [3].
[e]Reference [2].

VI. CONCLUSION

In summary, two main topics are discussed in this paper. First, the proton elastic scattering cross sections and analyzing powers from ^{90}Zr were investigated using a dispersive OMP, and the best-fit parameters were obtained at each energy. In this analysis, the geometrical parameters of the imaginary potential were allowed to vary; however, the volume integral of the imaginary potential at given energy was fixed to the value calculated from the analytical form of the imaginary potential energy dependence in the energy range from 9.8 to 135 MeV. The volume integral of the dispersive correction to the real central potential was calculated, based on the dispersion relation and a parametrization of the volume integral of the imaginary potential, and was fixed in the best-fit parameter search. The results of our analysis show that a similar reproduction of the data can be obtained in both conventional and dispersive OMP analyses.

The second study we present here obtained the mean field from the dispersion analysis, which is represented by a set of dispersive OMP parameters with smooth energy dependences. These mean-field parameters give good predictions for elastic cross section and analyzing power data in the energy range from 9.8 to 185 MeV. Predictions for single-particle and hole energies (as low as −60 MeV), rms radii, occupancies, spectroscopic factors, expectation values of the effective mass and spectral functions of the particle and hole states are presented.

ACKNOWLEDGMENTS

We would like to thank Dr. P. Schwandt for providing us with proton-^{90}Zr elastic cross section and analyzing power data. One of us (R.D.P.) would like to thank the support received from Research Experience for Undergraduates (REU) program sponsored by the National Science Foundation and the Department of Physics at Indiana University. This work was supported in part by the National Science Foundation.

[1] C. Mahaux and R. Sartor, in *Advances in Nuclear Physics,* edited by J. W. Negele and Erich Vogt (Plenum, New York, 1991), p. 1; C. H. Johnson and C. Mahaux, Phys. Rev. C **38**, 2589 (1988); C. Mahaux and H. Ngô, Nucl. Phys. **A378**, 205 (1982).

[2] C. H. Johnson, D. J. Horen, and C. Mahaux, Phys. Rev. C **36**, 2252 (1987).

[3] C. Mahaux and R. Sartor, Nucl. Phys. **A503**, 525 (1989).

[4] J. P. Delaroche, Y. Wang, and J. Rapaport, Phys. Rev. C **39**, 391 (1989).

[5] W. Tornow, Z. P. Chen, and J. P. Delaroche, Phys. Rev. C **42**, 693 (1990).

[6] C. Mahaux, H. Ngô, and G. R. Satchler, Nucl. Phys. **A449**, 354 (1986).

[7] Y. Wang, C. C. Foster, E. J. Stephenson, Li Yuan, and J. Rapaport, Phys. Rev. C **45**, 2891 (1992).

[8] R. D. Lawson, P. T. Guenther, and A. B. Smith, Nucl. Phys. **A493**, 267 (1989).

[9] C. H. Johnson, R. F. Carlton, and R. R. Winters, Phys. Rev. C **39**, 415 (1989).

[10] C. Mahaux and R. Sartor, Phys. Rev. C **36**, 1777 (1987).

[11] S. Chiba, P. T. Guenther, A. B. Smith, M. Sugimoto, and R. D. Lawson, Phys. Rev. C **45**, 1260 (1992).

[12] A. B. Smith, P. T. Guenther, and R. D. Lawson, Nucl. Phys. **A455**, 344 (1986).

[13] S. Chiba, P. T. Guenther, R. D. Lawson, and A. B. Smith, Phys. Rev. C **42**, 2487 (1990).

[14] R. W. Finlay, J. Wierzbicki, R. K. Das, and F. S. Dietrich, Phys. Rev. C **39**, 804 (1989).

[15] R. K. Das and R. W. Finlay, Phys. Rev. C **42**, 1013 (1990).

[16] C. Mahaux and R. Sartor, Nucl. Phys. **A481**, 381 (1988).

[17] G. W. Greenlees, C. H. Poppe, J. A. Sievers, and D. L. Watson, Phys. Rev. C **3**, 1231 (1971).

[18] C. Glashausser, R. De Swiniarski, J. Goudergues, R. M. Lombard, B. Mayer, and J. Thirion, Phys. Rev. **184**, 1217 (1969).

[19] R. De Swiniarski, Dinh-Lien Pham, and G. Bagieu, Can. J. Phys. **55**, 43 (1977).

[20] M. P. Fricke, E. E. Gross, B. J. Morton, and A. Zucker, Phys. Rev. **156**, 1207 (1967).

[21] G. S. Mani, D. T. Jones, and D. Jacques, Nucl. Phys. **A165**, 384 (1971).

[22] H. Sakaguchi, M. Nakamura, K. Hatanaka, A. Goto, T. Noro, F. Ohtani, H. Sakamoto, and S. Kobayashi, Phys. Lett. **89B**, 40 (1979); RCNP Annual Report (1978), p. 12.

[23] P. Schwandt, H. O. Meyer, W. W. Jacobs, A. D. Bacher, S. E. Vigdor, M. D. Kaitchuck, and T. R. Donoghue, Phys. Rev. C **26**, 55 (1982); A. Nadasen, P. Schwandt, P. P. Singh, W. W. Jacobs, A. D. Bacher, P. T. Debevec, M. D. Kaitchuck, and J. T. Meek, *ibid.* **23**, 1023 (1981).

[24] W. J. Courtney and J. D. Fox, At. Data Nucl. Data Tables **15**, 141 (1975).

[25] C. E. Laird, David Flynn, Robert L. Hershberger, and Fletcher Gabbard, Phys. Rev. C **35**, 1265 (1987).

[26] G. Finkel, D. Ashery, A. I. Yavin, A. Boudard, G. Bruge, A. Chaumeaux, and M. Rouger, Phys. Rev. C **19**, 1782 (1979).

[27] J. P. Delaroche, Y. Wang, and J. Rapaport, Phys. Rev. C **34**, 2005 (1986).

[28] L. R. B. Elton, in *Nuclear Radii,* edited by H. Schopper (Springer-Verlag, Berlin, 1967), p. 5.

[29] A. H. Wapstra and G. Audi, Nucl. Phys. **A432**, 1 (1985).

[30] J. P. Jeukenne and C. Mahaux, Nucl. Phys. **A394**, 445 (1983).

[31] P. Schwandt, Computer Code SNOOPY8Q, IUCF Internal Report No. 85-9.

[32] Y. Wang, computer code SNPQDR (1989), IUCF Internal Report No. 89-10 (unpublished).

[33] E. Hagberg, A. Ingermarsson, and B. Sundqvist, Phys. Scr. **3**, 245 (1971).

[34] Bruce D. Wilkins and George Igo, Phys. Rev. **129**, 2198 (1963); J. F. Dicello, G. J. Igo, and M. L. Roush, *ibid.* **157**, 1001 (1967); J. J. H. Menet, E. E. Gross, J. J. Malanify, and A. Zucker, Phys. Rev. C **4**, 1114 (1971); P. Kirkby and W. T. Link, Can. J. Phys. **44**, 1847 (1966); A. Johansson, U. Svanberg, and O. Sundberg, Ark. Fys. **19**, 527 (1961).

[35] J. W. A. den Herder, H. P. Blok, E. Jans, P. H. M. Keizer, L. Lapias, E. N. M. Quint, G. van der Steenhoven, and P. K. A. de Witt Huberts, Nucl. Phys. **A490**, 507 (1988).

[36] A. Stuirbrink, G. J. Wagner, K. T. Knopfle, Liu Ken Pao, G. Mairle, H. Riedesel, K. Schindler, V. Bechtold, and L. Friedrich, Z. Phys. A **297**, 307 (1980).

[37] K. Bharuth-Ram, A. C. Bawa, and W. R. McMurray, Phys. Rev. C **36**, 1749 (1987).

[38] J. L. Horton, C. L. Hollas, P. J. Riley, S. A. A. Zaidi, C. M. Jones, and J. L. C. Ford, Jr., Nucl. Phys. **A190**, 362 (1972).

[39] G. Finkel, D. Ashery, A. I. Yavin, G. Bruge, and A. Chaumeaux, Nucl. Phys. **217**, 197 (1973).

[40] P. D. Kunz, code DWUCK4 (unpublished).

[41] J. W. Negele and D. Vautherin, Phys. Rev. C **5**, 1472 (1972).

[42] M. G. E. Brand, G. A. Rijsdijk, F. A. Muller, K. Allaart, and W. H. Dickhoff, Nucl. Phys. **A531**, 253 (1991).